Progressive Damage Analysis of Carbon Fabric-reinforced Polymer Composites under Three-point Bending

Kang-ning Han, Wei Zhou*, Reng Qin, Sa Yang, and Lian-Hua Ma*

College of Quality and Technical Supervision, Hebei University, Baoding 071002, China

Abstract: Damage evolution of carbon fabric-reinforced polymer composite with various off-axis angles during the progressive bending tests was monitored by acoustic emission and Micro-CT. Meanwhile, the acoustic emission signals can be post-processed by *k*-means clustering methods. The results indicate that the maximum load and stiffness of laminates decrease with the increase of off-axis angle. Three key points (linear growth point, maximum load point and fail point) are selected to research the progressive damage. The existence of the Kaiser effect is observed. With the increase of off-axis angle, the damage degree and the load shared by the elastic-plastic matrix increase. The bending of matrix can enhance the fracture toughness and restrain the damage. The complementary technology can provide a basis for health monitoring of CFRP laminates.

Keywords: Carbon fiber, Carbon nanotubes, Three-point bend progressive damage, Acoustic emission, Micro-CT

Introduction

Carbon fabric-reinforced polymer (CFRP) composites have unique properties which makes them widely used in high-performance space, automotive structures and aerospace industries [1,2]. The weight of CFRP composite laminates has been substantially reduced owing to their high stiffness and strength to weight ratios. However, the CFRP composites are particularly susceptible to various damages such as bending and tensile damage. The strength, stiffness and energy-absorbing capability of CFRP composites can be affected by such damages within the materials. As one of the strongest and stiffest materials, carbon nanotubes (CNTs) can be incorporated into polymer matrix composites to improve the strength [3].

As an efficient method, acoustic emission can monitor and record the damage within the composite laminates in-situ and on-line in real-time [4-7]. Saeedifar *et al*. [8] used acoustic emission to investigate the barely visible impact damage in isotropic carbon/epoxy composite specimens under quasi-static indentation and low speed impact loading. Meanwhile, they utilized b-value and sentry function methods to analyze acoustic emission signals obtained during indentation tests and study the evolution of inter-laminar damages. It was indicated that acoustic emission can study the barely visible impact damage in laminates under quasi-static and dynamic loading powerfully. To analyze the damage accumulation and evolution during the process of the progressive damage, many studies have been carried out [9]. Zhang *et al*. [10] used acoustic emission and micro-computed tomography (Micro-CT) methods to study the influence of fiber direction through progressive three-point

bending tests. There was a good correlation between the microscopic damage morphology obtained through Micro-CT method and acoustic emission information. It was concluded that the longitudinal load bearing specimens had superior bearing capacity and deformation resistance because of the important supporting role of longitudinal fibers in the longitudinal bearing specimens.

Damages in composite laminates usually occur inside and are barely visible. To obtain full and comprehensive damage features, Micro-CT can be utilized to obtain the detailed 3D local features inside the composites non-destructively [11-15]. Micro-CT method can quantify the 3D micro-structure of CFRP composites in a few microns of spatial resolution and has been commonly used in materials science [16]. Micro-CT was employed in medical imaging originally and now has been widely used in composite laminates and mechanical structures. As a non-destructive testing technique, it can obtain the damage such as bubble defect, matrix cracks, kink band, delamination and fiber breakage [17,18]. Zhou *et al*. [19] studied the failure behaviour and damage mechanisms of carbon/aramid hybrid woven composites with different fibre orientations during the three-point bending tests by AE, infrared thermography (IRT) and Micro-CT. It was concluded that Micro-CT method enables the visualisation of the inner damage of composite. A comprehensive investigation of the damage and failure behaviour of composites can be realized combing with AE technology, IRT and Micro-CT. Suvarna *et al*. [20] studied the influence of temperature on post-impact bending and low speed impact resistance of carbon fiber composite laminates. The laminates with various temperatures were tested using the drop hammer to impact the tower at a speed of 2 m/s and using the three-point bending rig at environment temperature. At the same time, the ultrasonic C-Scan and Micro-CT were used to evaluate the impact and

*Corresponding author: zhouweihy@126.com
*Corresponding author: lhma@hbu.edu.cn

post-impact behaviors. The results indicated that inter-laminar fracture toughness was strongly influenced by temperature during low velocity impact tests and the delamination showed larger extent at low temperature.

Currently, many investigations are aimed at the damage evolution of CFRP composite laminates with CNTs in tension [21,22], flexure [21] and compression [23]. However, the effect of the off-axis angles on the progressive damages of CFRP laminates containing CNTs is not understood completely. In this research, to study the effect of off-axis angle during the progressive three-point bending tests, the acoustic emission was used to obtain the damage signals in real-time. At the same time, Micro-CT was utilized to measure the progressive damage of CFRP laminates according to 3D reconstructed images. The complementary technology including the acoustic emission and Micro-CT can provide a basis for health monitoring of CFRP laminates.

Experimental

Materials

The CFRP laminates were prepared with 12 layers of plain-weave carbon fiber by hand lay-up method [24]. Each ply of laminates consists of a plain-weave T300-3k carbon fabric. Figure 1 shows the schematic of CFRP laminates fabrication. A moderate amount of alcohol and MWCNTs with weight percentages of 0.5 wt% were added to a beaker. Then, the beaker was placed in an ultrasonic oscillator with a frequency of 40 kHz, and ultrasonic treatment was carried out at 30 °C for 2 hours to minimize the opportunities for aggregation. The epoxy resin was poured into the beaker and mixed uniformly. To remove the alcohol, the mixed liquid was sonicated for 10 h at 80 °C to ensure that the ethanol had completely evaporated. The mixture was placed in a cold water stream until the temperature reached environment temperature. Then, amount of curing agent was added into the mixture. The mixing ratio between the epoxy resin and the hardener was 100:40. In order to mix evenly, the mixed liquid was stirred at high speed for 20 minutes. The mixed liquid was treated in a vacuum oven for degassing treatment and spread evenly on each layer of plain woven fiber. The laminates were pressurized in mold by vacuum assisted resin transfer molding technology for 64 hours to solidify. The thickness of the laminate was 3±0.1 mm.

After roasting for 6 h at 130 °C and cooling down to room temperature, CFRP laminates was cut into standard specimens with different axial angles by Water-jet cutting method. The axial angles of Specimen A, B and C are 0 °, 30 ° and 45 °, respectively. The architectures of specimens with different axial angles are shown in Figure 2. The size of standard specimen is 60 mm×20 mm. Figure 3 shows the morphology features of Specimen A, B and C. There are three specimens in each class of composite materials.

Based on the information of supplier, the length of CNTs is about 7 μm and the CNTs have a diameter ranging 5-15 nm. The purity of CNTs is about 95 wt%. Figure 4(a) shows the morphology features of CNTs and Figure 4(b)
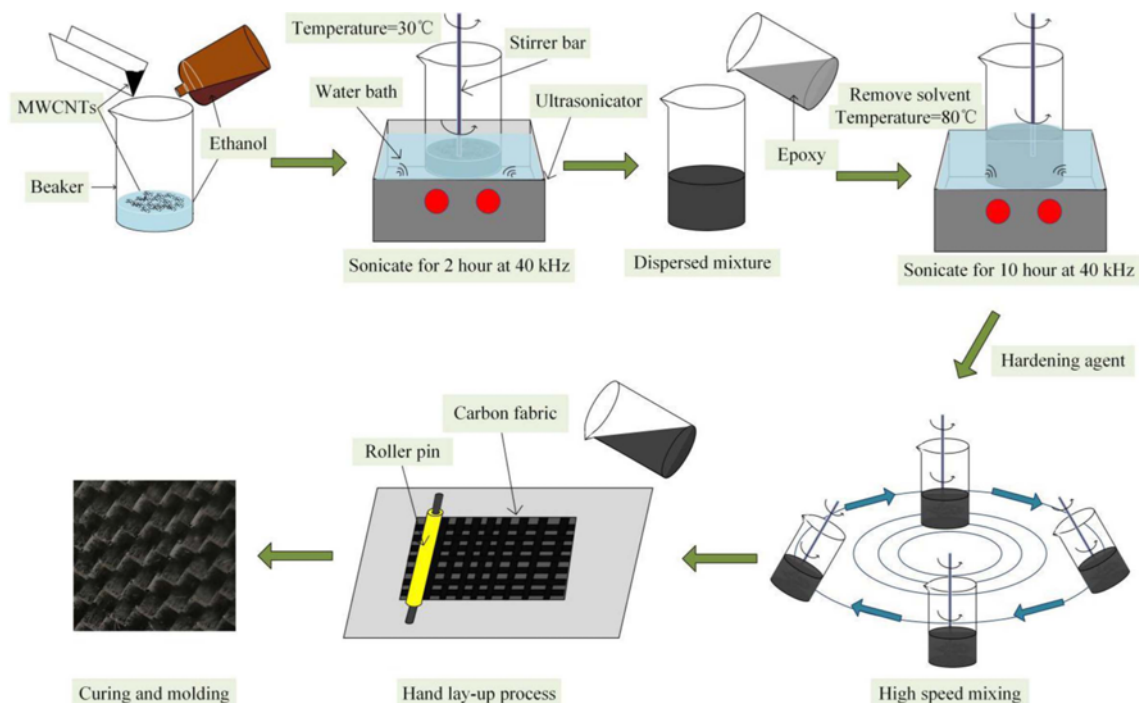

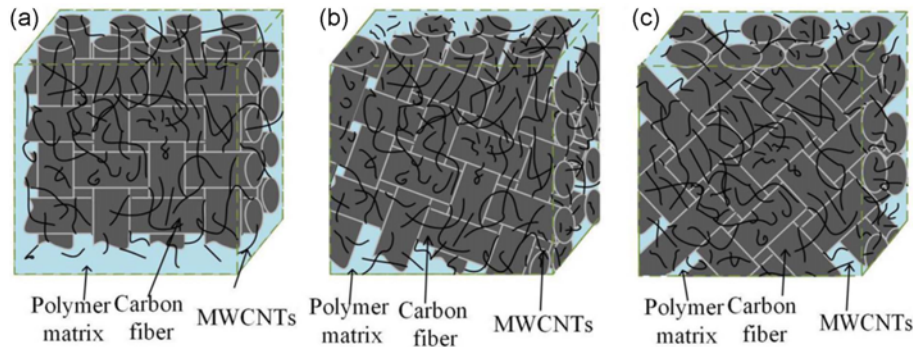**Figure 1.** Hand lay-up method of CFRP laminates.

Figure 2. Architectures of specimens with different axial angles; (a) specimen A (0 °), (b) specimen B (30 °), and (c) specimen C (45 °).
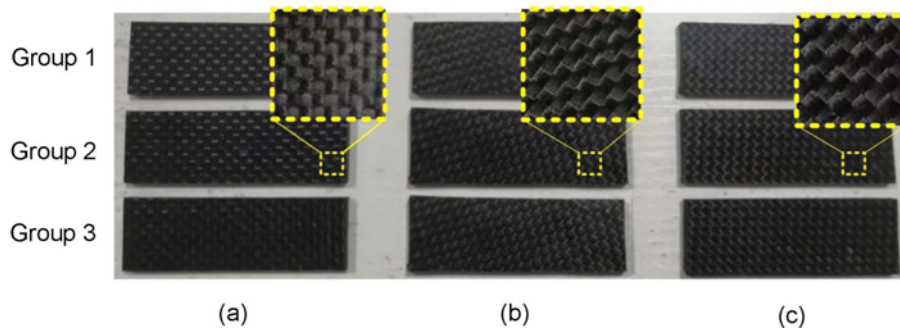

Figure 3. Three types of CFRP laminate specimens; (a) specimen A (0 °), (b) specimen B (30 °), and (c) specimen C (45 °).
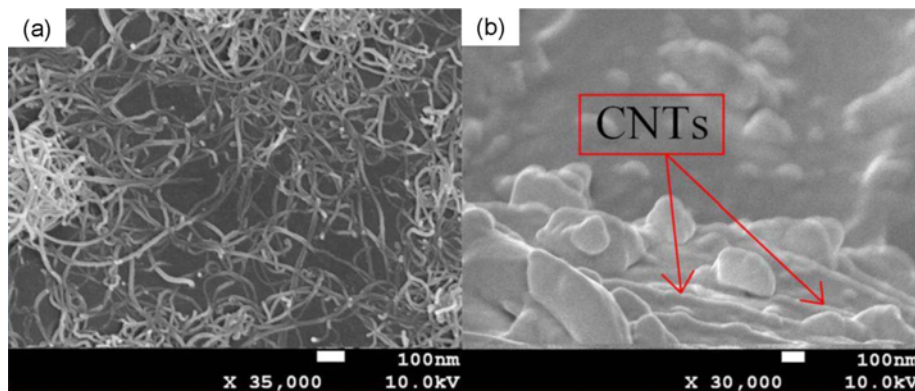

Figure 4. Microstructure characterization of CNTs; (a) morphology of CNTs and (b) morphology of CNTs in epoxy.

shows the morphology of CNTs in epoxy. The CNTs have the tube-shaped materials form and tend to create the agglomerations under the function of Van der Waals forces [25]. The microscopic mechanisms of CFRP laminates can be observed by SEM (JSM-7500F) which coated by gold before observation.

Testing

Three-point bending mechanical testing system is shown in Figure 5. According to ASTM D790, the three-point bending tests of CFRP laminate specimens were carried out on LD24 machine. The displacement loading rate was set as 2 mm/min. The distance of two supporting rollers was kept at 40 mm. An upper roller was located at the middle of composites to apply bending load. Acoustic emission instrument (DS2-8A) was used to acquire the acoustic emission signals during the process of three-point bending tests. Meanwhile, the peak definition time (PDT) was determined to be 30 μs, the hit definition time (HDT) was set to 150 μs and hit lock out time (HLT) to 300 μs. Two RS-54A acoustic emission sensors were installed on laminate specimens being 50 mm apart. The bandwidth of sensors is 100-900 kHz and the preamplifier is 40 dB. The sampling frequency and threshold were set as 3 MHz and 10 mV,
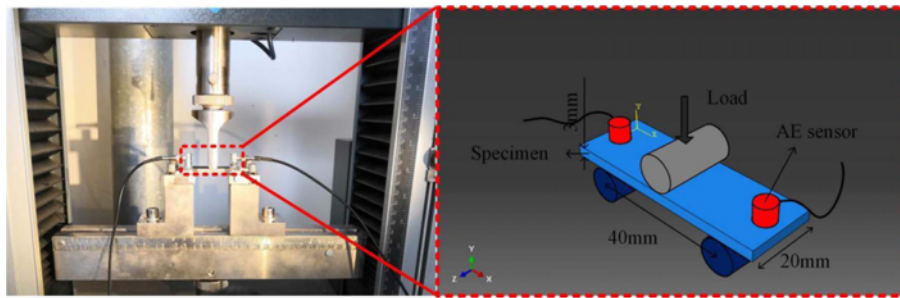
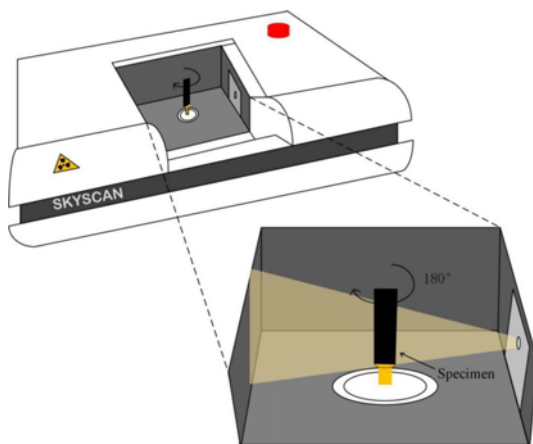**Figure 5.** Three-point bending mechanical testing system.

Figure 6. Measurement principle and apparatus of Micro-CT.

respectively. To have a good sound coupling, silicone grease and tape were used to fix the sensors on the surface of specimen.

Micro-CT Apparatus

The laminate specimens were scanned by Skyscan 1172 X-ray. Measurement principle and apparatus of Micro-CT are shown in Figure 6. 2D images were obtained with 180 ° of tomographic rotation (0.2 rotation step). For given size of the laminates and the distance between the laminate and X-ray source, high resolution image data with voxel size of 6.8 μm was generated. The X-ray tube voltage and beam current were set to 78 kV and 132 μA, respectively. The distance had been adjusted to ensure a specific region of interest of specimen on the detector screen. Each sample may use about 2 hours to acquire the images. The reconstruction was performed by NRecon based on Feldkamp algorithm. CT-vox software was utilized for 3D reconstruction model of the specimens. The components of the laminates were distinguishable based on the differences in the absorption of the X-ray radiation.

Progressive Three-point Bending Test

The mechanical curve was analyzed and three key points (linear growth point, maximum load point and fail point) were selected to analyze the progressive failure process according to the behaviors of CFRP laminates. When the loads achieved these key points, the test was paused and internal scanning was performed by Micro-CT system. Then, the specimens were moved back to the LD 24 machine and loaded until the next higher key point reached and re-recording the acoustic emission signals. Repeat the process until the specimens were eventually damaged.

Results and Discussion

Mechanical Characterization

Figure 7 exhibits the bending load-displacement curves of laminates with various off-axial angles. The failure loads of laminates with various off-axial angles are shown in Table 1. The average maximum loads of Specimen A, B and C are 1.45, 0.92 and 0.72 kN, respectively. The average bending strengths of Specimen A, B and C which calculated by equation (1) are 483.33, 306.67 and 240.00 MPa, respectively. The load-displacement curves exhibit good repeatability. Every curve can fully describe the initiation and growth of damage and the change of specimen stiffness. All curves
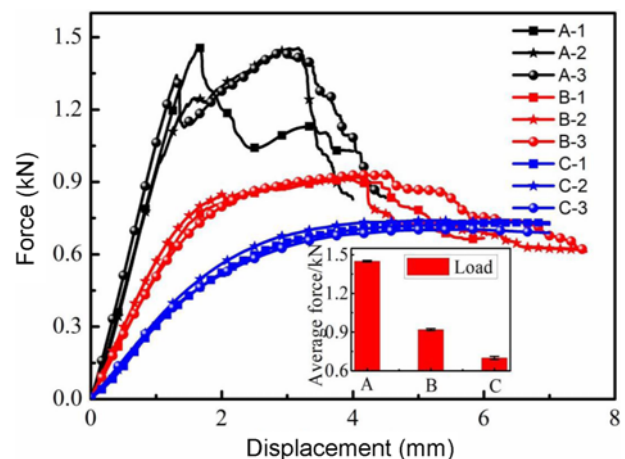

Figure 7. Bending load-displacement curves of laminates with various off-axial angles.

Table 1. Failure loads of laminates with various off-axial angles

	Load (kN)			Average value (kN)	Standard deviation (kN)	Bending strength (MPa)
	1	2	3			
Specimen A	1.46	1.45	1.45	1.45	0.006	483.33
Specimen B	0.91	0.92	0.93	0.92	0.008	306.67
Specimen C	0.73	0.74	0.70	0.72	0.013	240.00

show a linear growth trend at the beginning. However, the trend of curves of three laminates is significantly different with the bending load increasing, which indicates that the off-axis angles have an obvious impact on the failure mechanism. For both 0 ° and 30 ° specimens, a sudden drop is obtained when the first peak achieved. This phenomenon may be caused by the failure of the critical structure [26]. There is no sudden drop for 45 ° specimen owing to the matrix plasticity and alignment of tows along the loading directions which called fiber trellising [11]. With the increase of off-axis angle, the maximum load of the laminates decreases and the bending deflection increases. At the same time, the stiffness of laminates decreases with the increase of off-axis angle. The reason for this phenomenon may be that the fibers play an important supporting role

during bending process. The bottom fibers of specimens with 0 ° bear maximum tensile stress. Meanwhile, the specimens with 30 ° and 45 ° adjust themselves and change their spatial position through large geometric deformation [26].

$$R = \frac{3P_{max}L}{2bh^2} \qquad (1)$$

where b (mm) is the width of laminates. h (mm) is the thickness of laminates. P_{max} is the maximum load.

Acoustic Emission Characteristics

According to the Figure 7, three key points are selected to investigate progressive damage. In the linear stage, selecting the Point A (the linear growth point) to detect whether
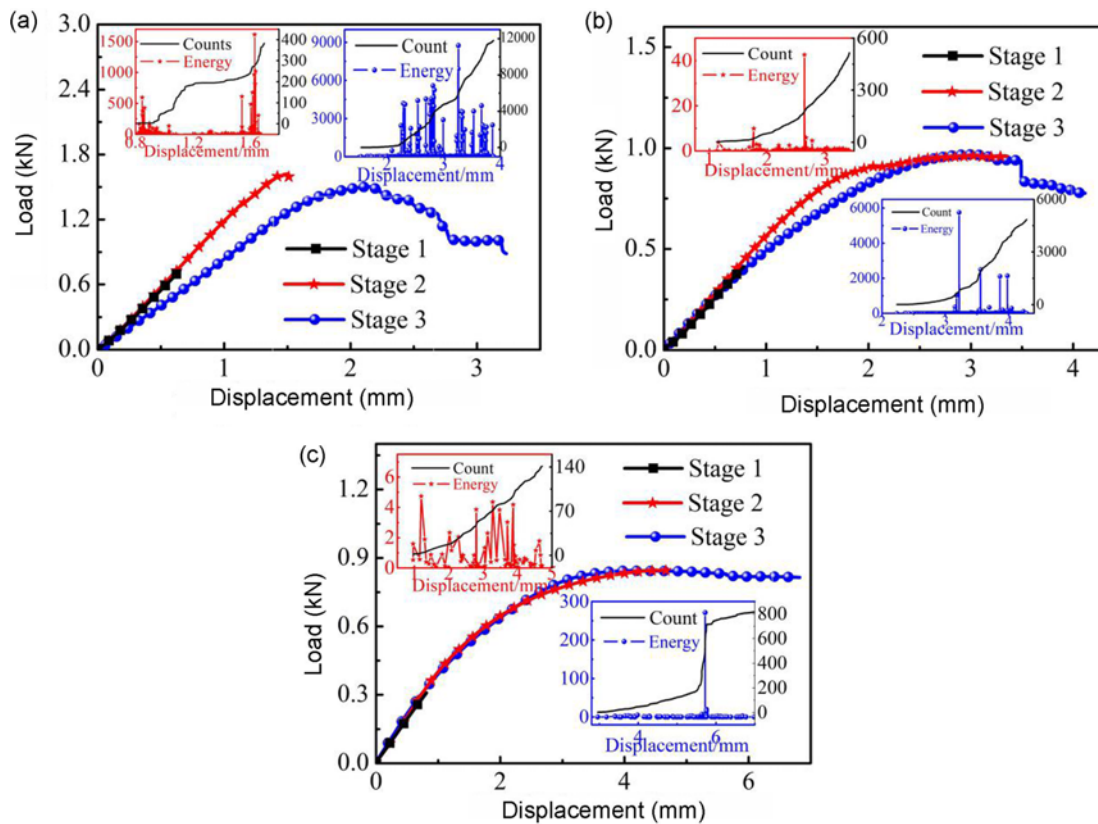

Figure 8. Progressive damage mechanical curves and acoustic emission character; (a) specimen A (0 °), (b) specimen B (30 °), and (c) specimen C (45 °).

initiation cracks have occurred. Point B is the maximum load point aiming to investigate the damage evolution. Point C is the fail point which is selected near the severe failure to study the characteristics during the serious damage state [10, 26]. Then, repeating three times at the same loading speed on the three points. Acoustic emission parameters (energy, counts, hits etc.) can be used to better understand the damage process [10]. The progressive damage mechanical curves and acoustic emission characters are shown in Figure 8. In Stage 1 (black line), the load and deflection exhibit linear relationship and no damages occurred. Acoustic emission signals are obtained in Stage 2 (red line) which is performed on the maximum load. In this stage, the maximum load and acoustic emission counts decrease with the off-axis angles increasing. The maximum energy values of Specimen A, B and C are 1612.62, 42.62 and 4.74 mV*mS, respectively. The specimens with small off-axis angle suffer more serious damage when they reach the maximum load. More acoustic emission signals are obtained in Stage 3 (blue line). However, an interesting observation indicates that there are no signals before Point B. This phenomenon shows the existence of stress memory-damage, which is consistent with the definition of the so-called Kaiser effect (KE) [10]. The definition of the KE is that acoustic emission signals are almost impossible to obtain until the previous maximum stress level is reached. Count and energy of all types of specimens increase significantly. The maximum energy value tend to decrease with the increase of off-axis angle. The acoustic emission signals obtained during the progressive damage are a mixture of signals corresponding to various damage modes. To better understand the damage mechanism of composites during progressive damage, principal component analysis and *k*-means cluster analysis are carried out to correlate the acoustic emission signals with different damage modes [27].

It is a very important step to distinguish the acoustic emission signals corresponding to various damage modes during loading process [10,27,28]. Figure 9 shows the *k*-means cluster analysis of specimens with various off-axis angles during Stage 2. 1-9 represent amplitude, frequency, RA value, impact number, time of duration, rise time, ringing count, rise count and energy, respectively. According
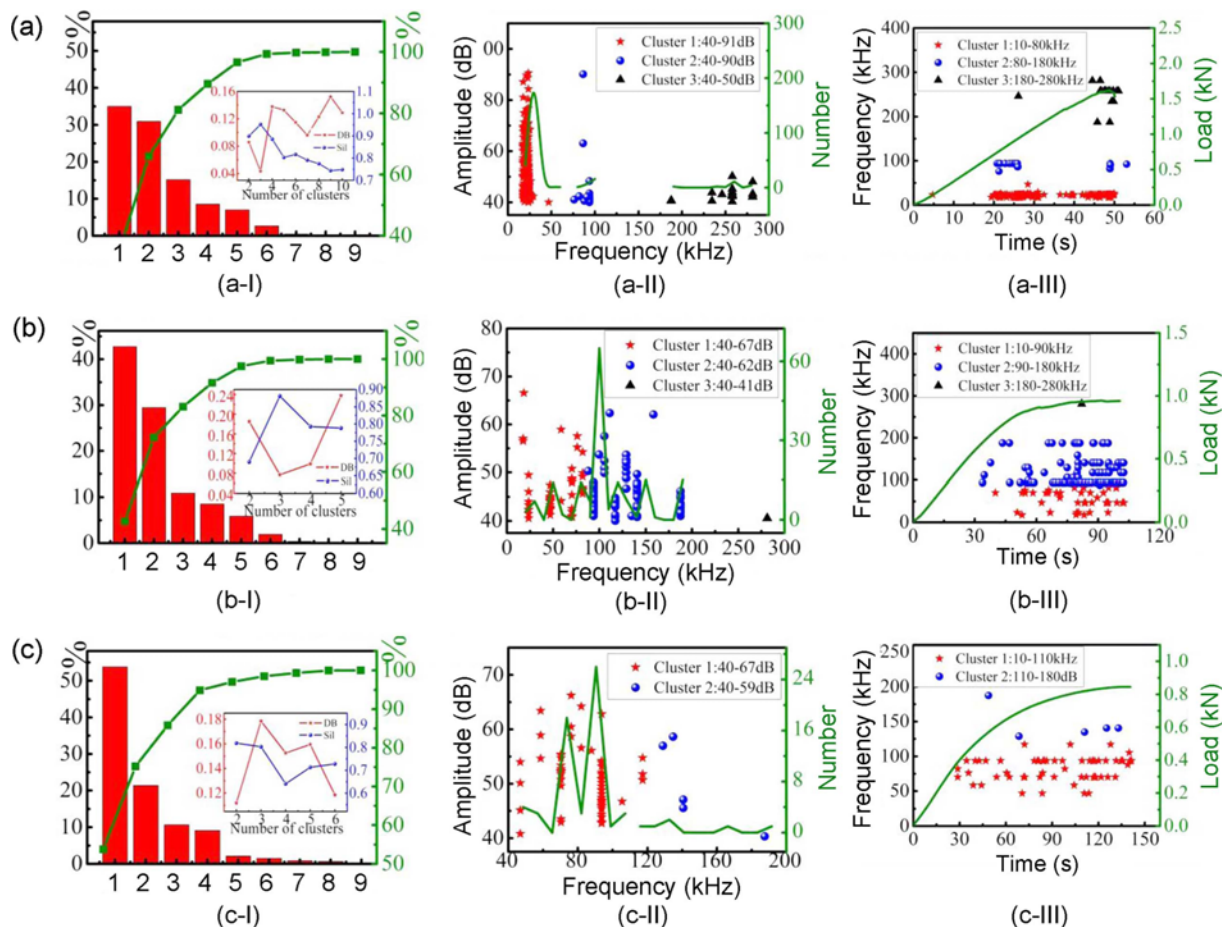

Figure 9. *k*-Mean cluster analysis of specimens with various off-axis angles during Stage 2; (a) specimen A (0°), (b) specimen B (30°), and (c) specimen C (45°).

to the results of principal component analysis, the percentage of the first three components is more than 80%, which can be used to conduct the optimal cluster number analysis. The lower DB value and higher Sil value represent the optimal number of clusters [27,28]. As seen from Figure 9, 3 is the optimal number of clusters in this stage according to Specimen A and B. For Specimen C, the optimal number of clusters can be set as 2. Frequency is an effective parameter and the range of frequency can represent a specific damage mechanism [10,27]. Cluster 1 represents matrix cracking, with the frequency range of about 10-90 kHz. Cluster 2 represents fiber debonding and delamination, with the frequency range of about 90-180 kHz. Cluster 3 represents fiber breakage, with the frequency range of about 180-280 kHz. With the increase of off-axis angles, the maximum amplitude of acoustic emission signals generated during the damage decrease slightly. For Specimen A, the signals of Cluster 1 and 2 are generated almost at the same time as the load increases. When it is about to reach the maximum load, a series of signals of fiber breakage occur simultaneously. For Specimen B, the signals of Cluster 1 and 2 continue to generate and the signals of Cluster 3 rarely occur in this

stage. For Specimen C, there are little signals generate and only two kinds of damage signals appear during the whole stage of loading which may be related to the plasticity. Furthermore, the damage is not as catastrophic as occurred in Specimen A [11].

Figure 10 shows the *k*-means cluster analysis of specimens with various off-axis angles during Stage 3. Similarly, according to the result of principal component analysis, the percentage of the first three components is more than 80 %, which can be used to conduct the optimal cluster number analysis. The optimal number of clusters for the three specimens in this stage is three according to Figure 10. Fiber breakage usually occurs at the last moment according to the general understanding of failure [5]. Cluster 1 represents matrix cracking, with the frequency range of about 10-90 kHz. Cluster 2 represents fiber debonding and delamination, with the frequency range of about 90-180 kHz. Cluster 3 represents fiber breakage, with the frequency range of about 180-280 kHz. Since Specimen A has higher strength and stiffness, besides, there are more fiber tows to bear the load simultaneously, the amplitude is relatively higher and the number of high frequency signals (fiber breakage) is larger
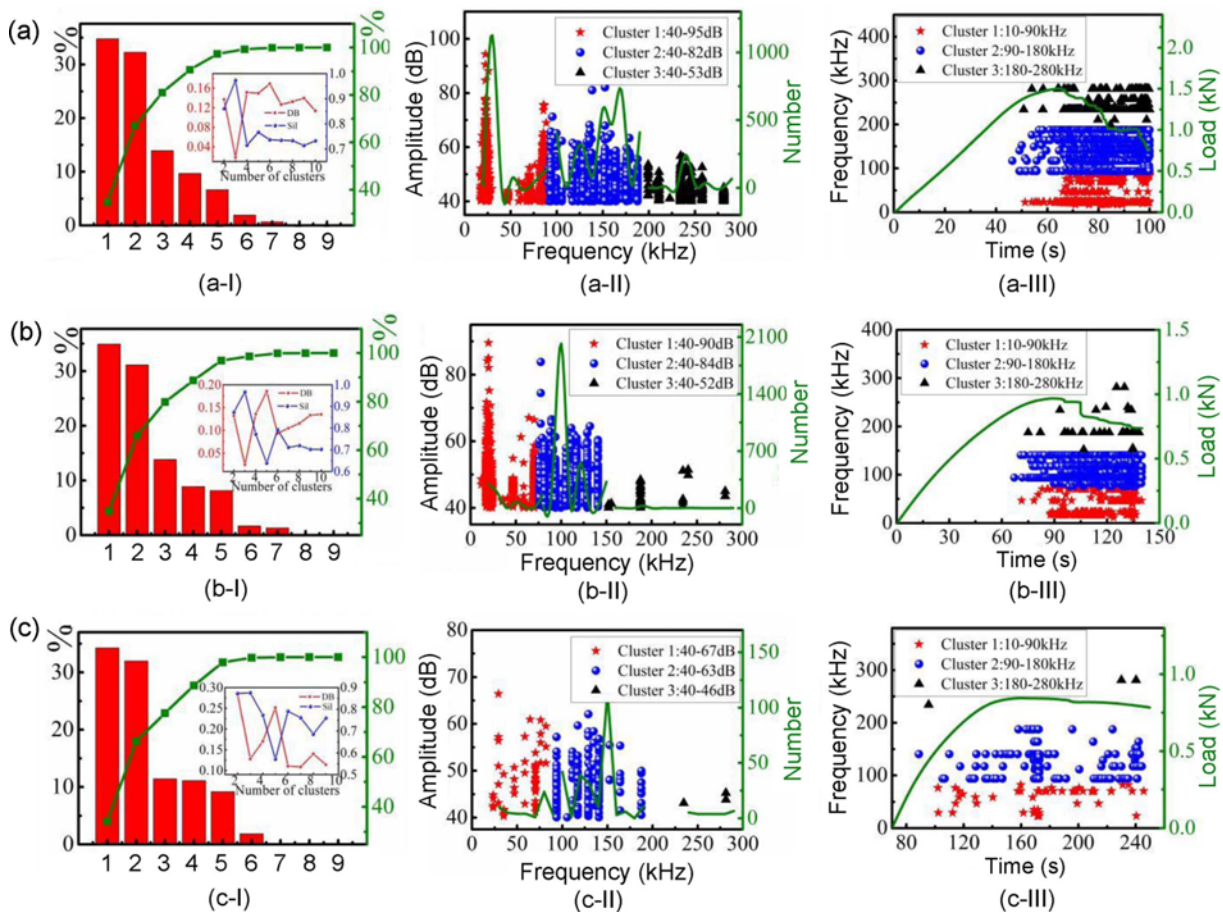

Figure 10. *k*-Mean cluster analysis of specimens with various off-axis angles during Stage 3; (a) specimen A (0°), (b) specimen B (30°), and (c) specimen C (45°).

than Specimen B and C. The brittle fracture of Specimen A and B is relatively obvious, which may be related to the simultaneous fracturing of fibers. Hence, the signals of fiber breakage are more than that of Specimen C. On the contrary, the pseudo-ductility of Specimen C leading to the damage is not catastrophic [11]. The acoustic emission parameters can character the damage evolution of CFRP laminates in real-time. To monitor the internal damage morphology, the

scanning tomography images are collected by Micro-CT.

Micro-CT Analysis

Micro-CT can monitor various damage modes of CFRP laminates at the micro-structure level [10]. The middle part of laminates is recorded due to the limitation of view field and the information obtained can be used to investigate the progressive failure process. Figure 11 demonstrates
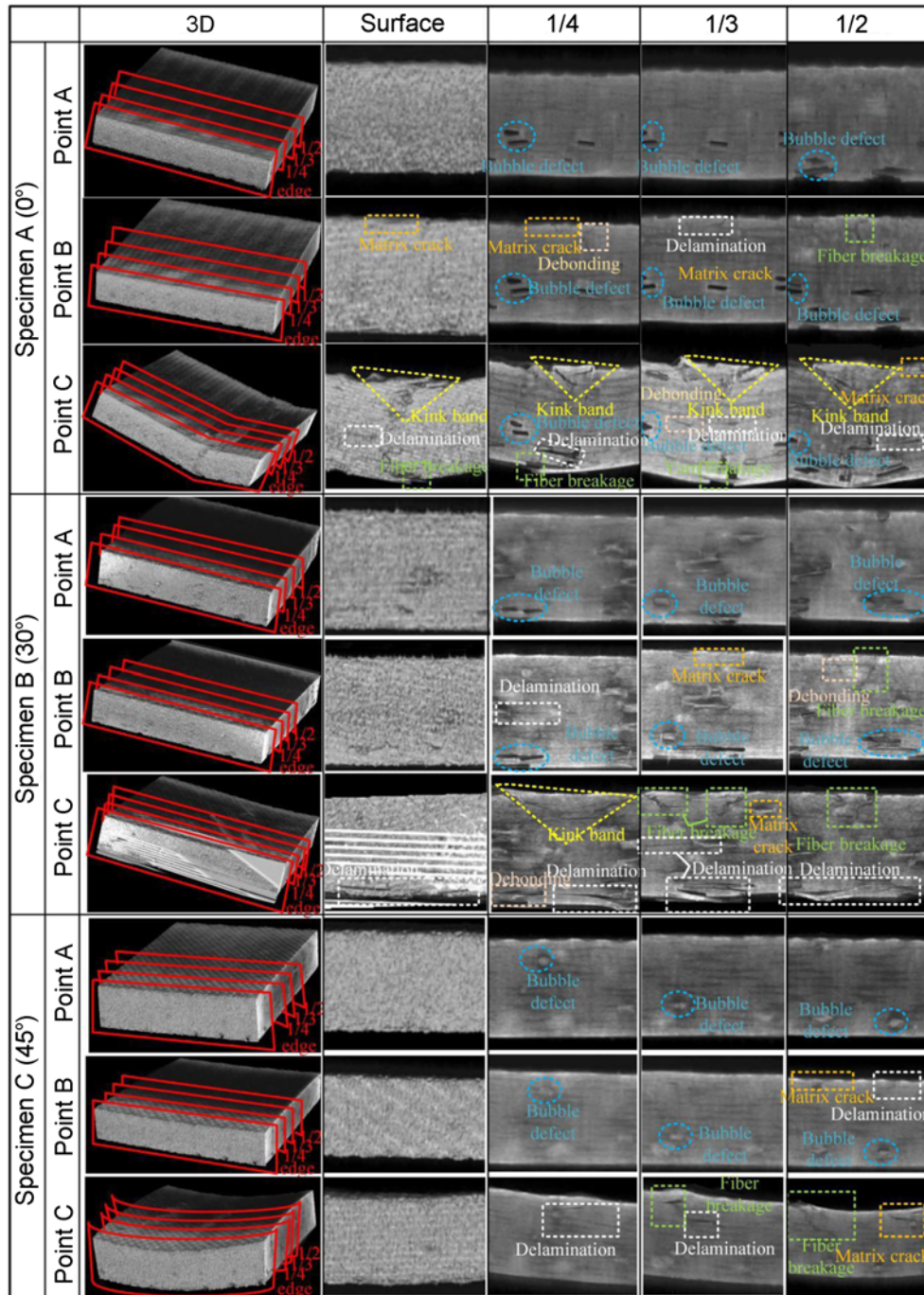

Figure 11. Tomographic sections of the damage mechanism at different stages with various off-axis angles.

tomographic sections of the damage mechanism at different stages with various off-axis angles. Higher-density materials have lighter colors, thus the light grey areas represent carbon fiber and dark grey areas represent cracks and damage [10, 26]. In Point A, the defects are mainly bubble defects which mainly come from the manufacture process and there is no obvious damage of three kinds of specimens. The damage initiation/evolution can be detected in the Stage 2. The load curve comes to Point B after the steep decline. In addition to bubble defect, the matrix crack, delamination and debonding almost occur in three kinds of specimens. The fiber breakage is found in Specimen A and B, which is consistent with the result of the cluster analysis of the acoustic emission signals as shown in Figure 9. However, the extent of damage decreases with the increase of off-axis angles apart from the similar damage modes. Micro-CT scan is carried out at Point C to obtain ultimate failure modes. In this point, the damage becomes more and more seriously. Damage to the matrix continues damaging the fibers through the coalescence of diffuse pores at the early period [2]. The elastoplastic matrix shares more loads with the increase of off-axis angles, thus bending occurs first which can enhance the fracture toughness and suppress damage. Because the damage is further deteriorated, the count and energy of signals increase as shown in Figure 8. For Specimen C, the fiber fracture is not as catastrophic as Specimen A and B due to plasticity. At the same time, the AE signals of Specimen C are less than

those of other specimens. Hence, it is evident that pseudo-ductility in Specimen C leads to the inhibition of damage under dynamic loading [11]. The damage from cross-section surface to 1/2 exhibits slight difference. Compared with the surface of the specimen, the middle part of the specimen has more comprehensive and severe damage. Hence, it can be reasonably inferred that damage initiation/evolution can be utilized by using the damage modes of 1/2 section rather than the damage modes of the whole specimen.

The details of the damage modes in the 1/2 section of specimens with different off-axis angles are shown in Figure 12. For Specimen A, the detailed failure modes mainly include kink band, fiber breakage, matrix crack, debonding and delamination. The fracture section is perpendicular to the fiber direction and the fiber damage penetrates the entire specimen with some fibers pulled out. The fracture occurs in a remarkably short period of time and leads to a sudden decreasing of load. Specifically, the kink band results in the high shear strain near the loading head due to fiber misalignment and matrix degradation [26]. Subsequently, cracks begin to appear in the matrix and fibers around the kink zone and the cracks propagate across the boundary toward another weft along the thickness direction. During this process, inter-tows cracks and debonding occur at warp and weft. Fibers are the dominant parts to bear the load which proves that the axial yarn have a supporting and reinforcing effect on the laminates. Therefore, Specimen A
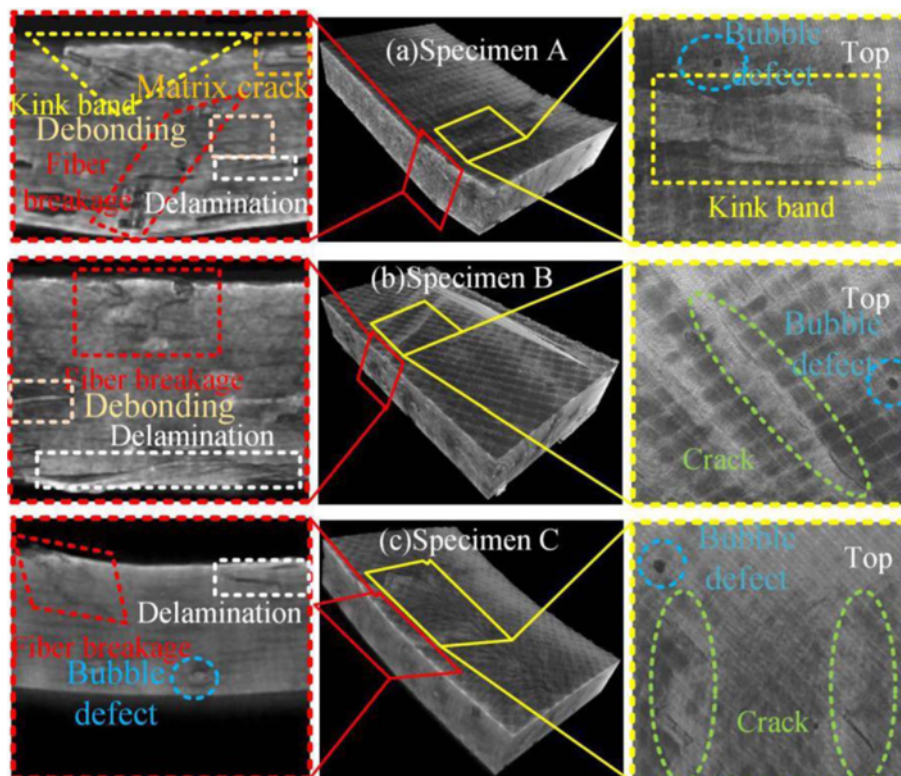

Figure 12. Damage modes in the 1/2 section of Point C of specimens with different off-axis angles.

has the largest failure load as shown in Figure 7. It can be obtained from the figure that the off-axis angle has significant influence on the damage evolution. With the decrease of the off-axis angle, the damage increases more and more severely. Unlike the characterization of Specimen A, the fiber breakage at the top and the delamination at the bottom are the main damages in Specimen B. No continuous cracks are found in these specimens. The fibers will slide when the fiber/matrix interface can not bear the shear stress which can result in the fiber/matrix cracking. For Specimen C, only a few fiber breakage and delamination appear at the top, which explains why the acoustic emission signals are shorter than those of Specimen A and B as shown in Figure 10. Moreover, the deformation and the load on matrix of Specimen C are lager. As a result, the bending strength of Specimen C is lower than that of others from a macroscopic level. In conclusion, Micro-CT can further verify the damage modes of laminates on the basis of acoustic emission technology. Acoustic emission technology can be utilized to monitor the damages inside the composites in real time. Micro-CT can analyze the damage modes in the process of progressive damage from the microscopic perspective. This complementary analysis method can provide a basis for health monitoring of CFRP laminates.

Conclusion

The progressive damage behaviors and failure mechanisms of CFRP laminates with various off-axis angles under bending load are investigated by a complementary technology including acoustic emission and Micro-CT. Some conclusions are summarized as follows:

1. The maximum loads and stiffness of laminates decreases with the increase of off-axis angles. A sudden drop is obtained when the first peak achieved for 0° and 30° specimens while there is no sudden drop for 45° specimen due to matrix plasticity and alignment of tows along the loading directions called fiber trellising.

2. Three key points (linear growth point, maximum load point and fail point) are selected to investigate the progressive failure process. The load and deflection exhibit linear relationship in Stage 1 and there are no damages occurred. In Stage 2, the degree of damage increases as the off-axis angles decreasing. The damage signals are divided into two clusters: matrix cracking, debonding and delamination. In Stage 3, the existence of the Kaiser effect (KE) and more acoustic emission signals are observed. The signals are divided into three clusters: matrix cracking, debonding and delamination, fiber breakage.

3. In Point A, there are few damages except for bubbles. In Point B, different damage modes can be detected, but the extent of damage decreases with the off-axis angles increasing. In Point C, bending occurs first because the elastoplastic matrix shares more loads with the increase of off-axis angles, which can enhance the fracture toughness and suppress damage. For Specimen A, the fracture sections are perpendicular to the fiber direction and the fiber damage penetrates the entire specimen with some fibers pulled out. For Specimen B, the main damages are fiber breakage at the top and the delamination at the bottom. For Specimen C, only a little fiber breakage and delamination appear at the top, furthermore, the fiber fracture is not as catastrophic as Specimen A and B due to plasticity.

4. Acoustic emission can record the damage in-situ and monitor the structural damage and failure in real time, Micro-CT can obtain the detailed 3D local features inside the composites. The complementary technology including the acoustic emission and Micro-CT can provide a basis for health monitoring of CFRP laminates.

Acknowledgements

References

1. Y. Wang, T. L. Burnett, Y. Chai, C. Soutis, P. J. Hogg, and P. J. Withers, *Compos. Struct.,* **160**, 917 (2017).
2. P. Chowdhury, H. Sehitoglu, and R. Rateick, *Carbon*, **126**, 382 (2018).
3. W. Y. Wan Hanif, M. S. Risby, and M. M. Noor, *Procedia Eng.,* **114**, 118 (2015).
4. L. Michalcova and M. Kadlec, *Eng. Fail. Anal.,* **69**, 88 (2016).
5. C. Huang, S. Ju, M. He, Q. Zheng, Y. He, J. Xiao, J. Zhang, and D. Jiang, *Compos. Struct.,* **206**, 70 (2018).
6. M. Saeedifar, M. A. Najafabadi, D. Zarouchas, H. H. Toudeshky, and M. Jalalvand, *Compos. Part B-Eng.,* **152**, 180 (2018).
7. W. Hao, Z. Yuan, C. Tang, L. Zhang, G. Zhao, and Y. Luo, *Compos. Struct.,* **208**, 141 (2019).
8. H. Ahn and W. R. Yu, *Compos. Struct.,* **160**, 1105 (2017).
9. G. Liu, L. Zhang, L. Guo, F. Liao, T. Zheng, and S. Zhong, *Compos. Struct.,* **208**, 233 (2019).
10. P. Zhang, W. Zhou, H. Yin, and J. Shang, *Compos. Struct.,* **226**, 111196 (2019).
11. H. Ullah, A. R. Harland, and V. V. Silberschmidt, *Mater. Des.*, **88**, 149 (2015).
12. J. M. Gebert, A. Wanner, R. Piat, M. Guichard, S. Rieck, B. Paluszynski, and T. Böhlke, *Mech. Adv. Mater. Struc.,* **15**, 467 (2008).
13. J. Ya, Z. Liu, and Y. Wang, *Appl. Compos. Mater.,* **24**, 593 (2017).
14. Y. Li, B. Sun, and B. Gu, *Compos. Struct.,* **176**, 43 (2017).

15. H. Wang and Z. Wang, *Appl. Compos. Mater.*, **23**, 601 (2016).

16. Y. Wang, T. L. Burnett, Y. Chai, C. Soutis, P. J. Hogg, and P. J. Withers, *Compos. Struct.,* **160**, 917 (2017).

17. K. T. Tan, N. Watanabe, and Y. Iwahori, *Compos. Part B-Eng.,* **42**, 874 (2011).

18. R. Suvarna, V. Arumugam, D. J. Bull, A. R. Chambers, and C. Santulli, *Compos. Part B-Eng.,* **66**, 58 (2014).

19. W. Zhou, H. F. Yin, Y. J. Shang, and P. F. Zhang, *Nondestruct. Test. Eva*., **35**, 139 (2020).

20. R. Suvarna, V. Arumugam, D. J. Bull, A. R. Chambers, and C. Santulli, *Compos. Part B-Eng.,* **66**, 58 (2014).

21. A. El Moumen, M. Tarfaoui, and K. Lafdi, *Appl. Compos. Mater.,* **25**, 569 (2018).

22. M. Tarfaoui, K. Lafdi, and A. El Moumen, *Compos. Part B-Eng.,* **103**, 113 (2016).

23. A. El Moumen, M. Tarfaoui, O. Hassoon, K. Lafdi, H. Benyahia, and M. Nachtane, *Appl. Compos. Mater.,* **25**, 309 (2018).

24. D. Kumar, K. K. Singh, and R. Zitoune, *Mech. Eng. B-J. Eng.*, **232**, 2533 (2018).

25. A. El Moumen, M. Tarfaoui, and K. Lafdi, *Compos. Part B-Eng.,* **114**, 1 (2017).

26. D. Zhang, X. Liu, Y. Gu, M. Sun, S. Yu, Y. Zhang, and K. Qian, *Compos. Part A-Appl. Sci. Manuf.*, **115**, 311 (2018).

27. W. Zhou, W. Zhao, Y. Zhang, and Z. Ding, *Compos. Struct.,* **195**, 349 (2018).

28. W. Zhou, K. Han, R. Qin, and Y. Zhang, *Mater. Res. Express*, **6**, 085624 (2019).